
Hairpin vortices and heat transfer in the wakes behind two hills with different scales

Hideki Yanaoka (柳岡英樹)*

Department of Systems Innovation Engineering,
Faculty of Science and Engineering, Iwate University,
4-3-5 Ueda, Morioka, Iwate 020-8551, Japan

Tatsuya Hamada (濱田達哉)

Mechanical Engineering,
Graduate School of Engineering, Iwate University,
4-3-5 Ueda, Morioka, Iwate 020-8551, Japan

July 17, 2023

ABSTRACT

This study performed a numerical analysis of the hairpin vortex and heat transport generated by the interference of the wakes behind two hills in a laminar boundary layer. In the case of hills with the same scale, the interference between hairpin vortices in the wake is more intensive than in the different-scale hills. When the hills with different scales are installed, hairpin vortices with different scales are periodically shed. Regardless of the scale ratio of the hills, when the hill spacing in the spanwise direction is narrowed, the asymmetry of the hairpin vortex in the wake increases due to the interference between the wakes. At this time, the turbulence caused by the leg and the horn-shaped secondary vortex on the spanwise center side in the hairpin vortex increases, and heat transport around the hairpin vortex becomes active. In addition, the leg approaches the wall surface and removes high-temperature fluid near the wall surface over a wide area, resulting in a high heat transfer coefficient. These tendencies are most remarkable in the same-scale hills. In the case of hills with different scales, the heat transfer coefficient decreases because the leg on the spanwise center side in a small hairpin vortex does not develop downstream.

Keywords Vortex dynamics, Hairpin vortex, Heat transfer, Unsteady flow, Boundary layer separation, Numerical simulation

1 Introduction

In the flow around protuberance, separation bubbles occur ahead and behind the protuberance, and a coherent vortex structure exists in the wake. In such a flow field, heat, substance, and momentum are actively transported by the vortex. Therefore, many studies have investigated the flow and the wake around a single protuberance (Acarlar and Smith, 1987; Sakamoto et al., 1987; Yang et al., 2001; Simpson et al., 2002; Dong and Meng, 2004; Yanaoka et al., 2007a,b, 2008) and multiple protuberances or cylinders (Ko et al., 1996; Sumner et al., 1999; Meinders and Hanjalić, 2002; Kurita and Yahagi, 2008).

When multiple protuberances are set in the flow, the wakes of the protuberances interfere with each other, resulting in complicated flows. Many studies have investigated interference between wakes behind multiple cylinders with the same or different diameters (Ko et al., 1996; Sumner et al., 1999; Kurita and Yahagi, 2008). However, although the flow around the protuberance has been clarified in the previous study for multiple three-dimensional protuberances (Meinders and Hanjalić, 2002), vortex structures in the wake and interference between wakes have not been investigated. Furthermore, in such a study on the flow around three-dimensional protuberances, protuberances with the same scale are used, and the wake behind protuberances with different scales has not been investigated.

In the wakes behind three-dimensional protuberances such as cubes (Yanaoka et al., 2007a), trapezoidal tabs (Dong and Meng, 2004), hemispheres (Acarlar and Smith, 1987; Yang et al., 2001), and hills (Simpson et al., 2002; Yanaoka et al., 2007b, 2008), it is known that there are three-dimensional vortex structures such as hairpin vortices. So far,

*Email address for correspondence: yanaoka@iwate-u.ac.jp

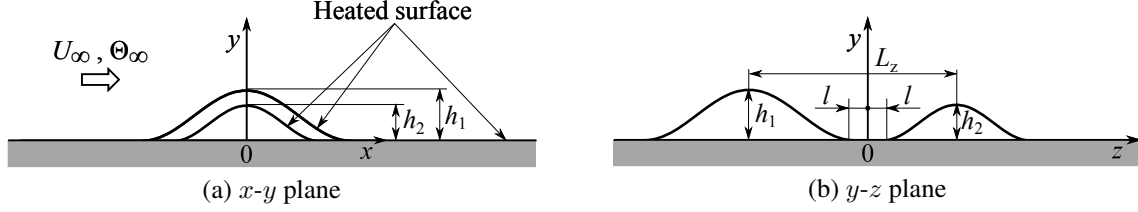


Figure 1: Flow configuration and coordinate system.

the authors (Yanaoka et al., 2007b) have performed a three-dimensional numerical analysis of the behavior and heat transfer of a hairpin vortex in the wake behind a single hill in a laminar boundary layer. It has been reported that hairpin vortices cause high turbulence in the wake and increase heat transfer. Li et al. (2019) investigated the coherent structure and heat transfer in the turbulent boundary layer along a channel wall with a rib tabulator and found that multiple hairpin vortices occur, increasing the heat transfer coefficient and turbulence. When such three-dimensional protuberances are installed side by side in a flow field, the three-dimensional vortex structure in the wake is deformed by the interference between the wakes. Therefore, it is considered that the characteristics of turbulence and heat transfer change significantly compared to the case of a single protuberance. Furthermore, in the case of protuberances with different scales, the wakes with different scales interfere with each other. Thus, it is considered that the characteristics of the three-dimensional vortex structure, turbulence, and heat transfer in the wake are different from the characteristics of the flow around the protuberances with the same scale.

From the above viewpoints, this study investigates the interference between the wakes behind the hill-shaped protuberances in a laminar boundary layer to clarify the effects of the hill spacing and scale ratio on the hairpin vortex structure and heat transfer in the wakes behind two hills.

2 Fundamental equation and numerical procedures

Figure 1 shows the flow configuration and coordinate system. The origin is on the wall surface, and the x -, y -, and z -axes are the streamwise, cross-streamwise, and spanwise directions, respectively. The velocities in these directions are denoted as u , v , and w , respectively, and the temperature is denoted as θ . A uniform flow originates upstream and a laminar boundary layer develops downstream. The free stream velocity and temperature are denoted as U_∞ and Θ_∞ , respectively. In this study, similar to Acarlar and Smith (1987), a protuberance is placed in the laminar boundary layer, and a hairpin vortex is generated by using flow separation. The protuberance has the same shape as that used in the experiment of Simpson et al. (2002). The height shapes of the two hills are given as follows:

$$\frac{y(r_k)}{h_1} = -\frac{1}{6.04844} \left[J_0(\Lambda) I_0 \left(\Lambda \frac{r_k}{a_k} \right) - I_0(\Lambda) J_0 \left(\Lambda \frac{r_k}{a_k} \right) \right], \quad (1)$$

where $\Lambda = 3.1926$, r_k ($k = 1, 2$) is the radius, h_k is the hill height, $a_k = 2h_k$ is the hill radius, J_0 is the Bessel function of the first kind, and I_0 is the modified Bessel function of the first kind. The vertices of two hills are placed on the z -axis, and the distance between two hills in the spanwise direction is L_z . The radius r_k is given, respectively, as follows:

$$r_1 = \sqrt{x^2 + (z + 2h_1 + l)^2} \quad \text{if } (z < 0), \quad (2)$$

$$r_2 = \sqrt{x^2 + (z - 2h_2 - l)^2} \quad \text{if } (z \geq 0), \quad (3)$$

where l is the distance from the bottom of the hill to the origin and is given as $l = (L_z - a_1 - a_2)/2$.

This study deals with the three-dimensional flow of an incompressible viscous fluid with constant physical properties. The continuity, Navier-Stokes, and energy equations in Cartesian coordinates are transformed into those to a general coordinate system. The governing equations are solved using the simplified marker and cell method (Amsden and Harlow, 1970) extended to the collocated grid. The pressure interpolation proposed by Rhie and Chow (1983) is used to remove spurious errors. The Crank–Nicolson method is applied to discretize the time derivative and then time marching is performed. The second-order central difference scheme is used to discretize the spatial derivative.

3 Details of calculation

In this study, we consider the cases where the scale ratio of two hills is $h_2/h_1 = 1$ and $7/8$, and the hill spacing is $L_z = 4h_1$ and $5h_1$. We adjusted the scale ratio so that a small-scale hairpin vortex was formed behind the hill at

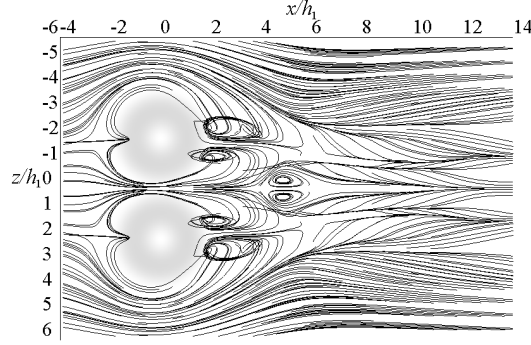


Figure 2: Time-averaged streamlines at $y/h_1 = 0.1$ for $h_2/h_1 = 1$ and $L_z = 4h_1$.

$z/h_1 \geq 0$ for $L_z = 4h_1$ and set $h_2/h_1 = 7/8$. In the smaller scale ratio, the hairpin vortex was not generated. The calculation region is from $-10h_1$ to $25h_1$ in the x -direction and 0 to $8h_1$ in the y -direction. To unify the distance from the center of the hill to the boundary in the spanwise direction, for $L_z = 4h_1$ and $5h_1$ of $h_2/h_1 = 1$, the calculation region in the z -direction is $-9h_1$ to $9h_1$ and $-9.5h_1$ to $9.5h_1$, respectively. For $L_z = 4h_1$ and $5h_1$ of $h_2/h_1 = 7/8$, the region in the z -direction is $-9.125h_1$ to $9.125h_1$ and $-9.625h_1$ to $9.625h_1$, respectively.

For the boundary conditions of the velocity field, the Blasius velocity profile is given at the inlet, and convective boundary conditions are used at the outlet. No-slip boundary conditions are applied on the walls. Slip boundary conditions are assumed at the upper boundary away from the bottom surface and at the boundary in the spanwise direction. For the boundary condition of the temperature field, a uniform temperature is given at the inlet, and the convective boundary condition is used at the outlet. The hill surface and bottom wall are heated with a constant heat flux. A zero gradient of the temperature is assumed at the upper boundary and in the spanwise direction.

The numerical calculations are performed under the Reynolds number $Re = 500$ defined by h_1 and U_∞ , and the Prandtl number $Pr = 0.7$. The velocity boundary layer thickness δ at the inlet is set so that the thickness δ becomes $\delta_0/h_1 = 1$ at $x/h_1 = 0$ without the hill. These conditions are the same as the previous calculation (Yanaoka et al., 2007b).

To confirm the grid dependency on the calculation result, we use the four grids for $h_2/h_1 = 1$ and three grids for $h_2/h_1 = 7/8$. For $h_2/h_1 = 1$, grid points of $181 \times 56 \times 133$ (grid1), $256 \times 70 \times 151$ (grid2), $300 \times 80 \times 169$ (grid3), and $335 \times 90 \times 179$ (grid4) are used. For $h_2/h_1 = 7/8$, grid points of $181 \times 56 \times 133$ (grid1), $256 \times 70 \times 151$ (grid2), and $335 \times 90 \times 179$ (grid3) are used. The grids are dense near the lower wall surface and hills. For each h_2/h_1 , we investigated the influence of the number of grid points on the calculation results for $L_z = 4h_1$, where the turbulence is the highest. We will describe the grid dependency later. In this study, to clarify the turbulence due to the vortex structure in more detail, the calculation results using grid4 and grid3 are mainly shown for $h_2/h_1 = 1$ and $7/8$, respectively.

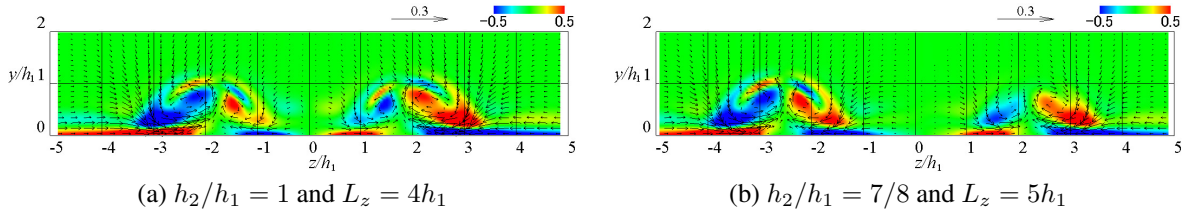
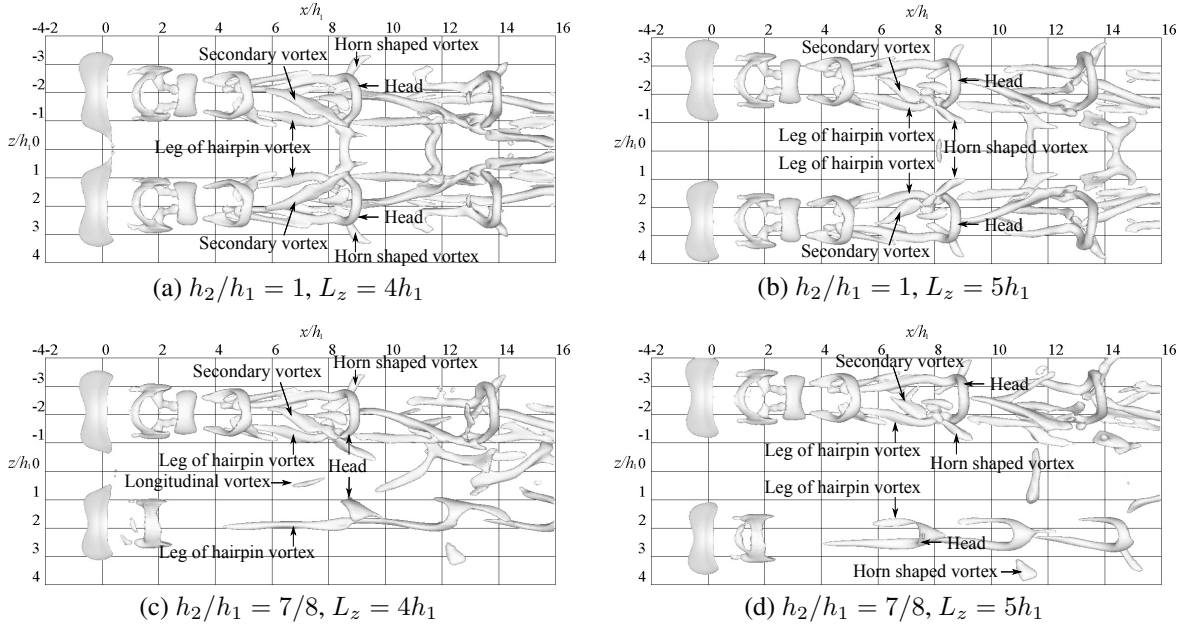
4 Results and discussion

4.1 Flow around hills

Figure 2 shows the streamlines of the time-averaged flow in the x - z cross-section for $h_2/h_1 = 1$ and $L_z = 4h_1$. The results of other conditions were similar to the results of $h_2/h_1 = 1$ and $L_z = 4h_1$, so they are omitted here. A pair of vortices are formed behind the hill. This vortex pair is similar to the CVP (Counter-rotating Vortex Pair) observed in the visualization experiment on the flow around a tab-shaped obstacle by Elavarasan and Meng (2000).

As a contraction flow occurs between the hills and the pressure decreases, the fluid is drawn toward the center $z/h_1 = 0$ of the spanwise direction, and the separation bubbles move to the spanwise center. The movement of the separation bubble to the spanwise center reduces the size of the recirculation region on the spanwise center side compared to the result for a single hairpin vortex (Yanaoka et al., 2007b). As a result, the vortex pair behind the hill becomes asymmetric to the center plane of the hill.

Figure 3 shows the instantaneous streamwise vorticity contours and velocity vectors in the y - z plane. Under each condition, vortex pairs that rotate in opposite directions are asymmetrically formed behind the hills. In all cases, vorticity is low on the spanwise center side of the vortex pair, and flow circulation weakens. For each h_2/h_1 , when the hill spacing is narrowed, the magnitude of the vorticity on the spanwise center side in the vortex pair at $z/h_1 \geq 0$ becomes lower. This tendency is remarkable for $h_2/h_1 = 7/8$ and $L_z = 4h_1$.


 Figure 3: Streamwise vorticity contours and velocity vectors in y - z plane at $x/h_1 = 3.0$.

 Figure 4: Isosurface of curvature of equipressure surface: Isosurface value is $-7/h_1$.

4.2 Vortex structures in the wake

Figure 4 shows the isosurface of the curvature calculated from the equipressure surface to clarify the vortex structure existing in the flow field. To compare the instantaneous vortex structures in the same state for each condition, we show the flow field when the head center of a hairpin vortex shed from the hill at $z/h_1 < 0$ passes through $x/h_1 = 5$. The position where the pressure of the head became minimum was defined as the head center. In the flow field, there exist the head and leg of a hairpin vortex, the secondary vortex, the horn-shaped secondary vortex, and the longitudinal vortex. In each figure, these vortex structures are labeled. Under all conditions, the shear layer separated at the top of the hill becomes unstable downstream and rolls up into a vortex. This vortex grows into a hairpin vortex and is periodically shed downstream.

For $h_2/h_1 = 1$, the hairpin vortices around $x/h_1 = 4 - 5$ are similar to the existing result (Yanaoka et al., 2007b). However, the hairpin vortices existing at $x/h_1 = 6 - 9$ become asymmetrical due to the interference of the vortices with each other, which is different from the previous result (Yanaoka et al., 2007b). Around $x/h_1 = 6 - 8$, a secondary vortex is generated between both legs of the hairpin vortex. This secondary vortex develops above the leg on the spanwise center side as it moves downstream. A horn-shaped secondary vortex occurs under the hairpin vortex. These horn-shaped secondary vortices have also been observed in the previous study (Yanaoka et al., 2007b). The horn-shaped secondary vortices on the spanwise center side spread in the spanwise direction with time and are coupled to each other downstream. In the case of $L_z = 4h_1$, it can be seen that horn-shaped secondary vortices are connected around $x/h_1 = 8.5$. As the hill spacing at $L_z = 5h_1$ is wider than at $L_z = 4h_1$, it is observed that they are combined at $x/h_1 = 11.5$ further downstream. In existing studies using two-dimensional cylinders (Sumner et al., 1999; Kurita and Yahagi, 2008), it was observed that the flow field was symmetrical to the spanwise direction when the cylinder spacing was wide. On the other hand, it was observed that the flow field became asymmetric when the cylinder spacing was narrow. A similar tendency appears in this study.

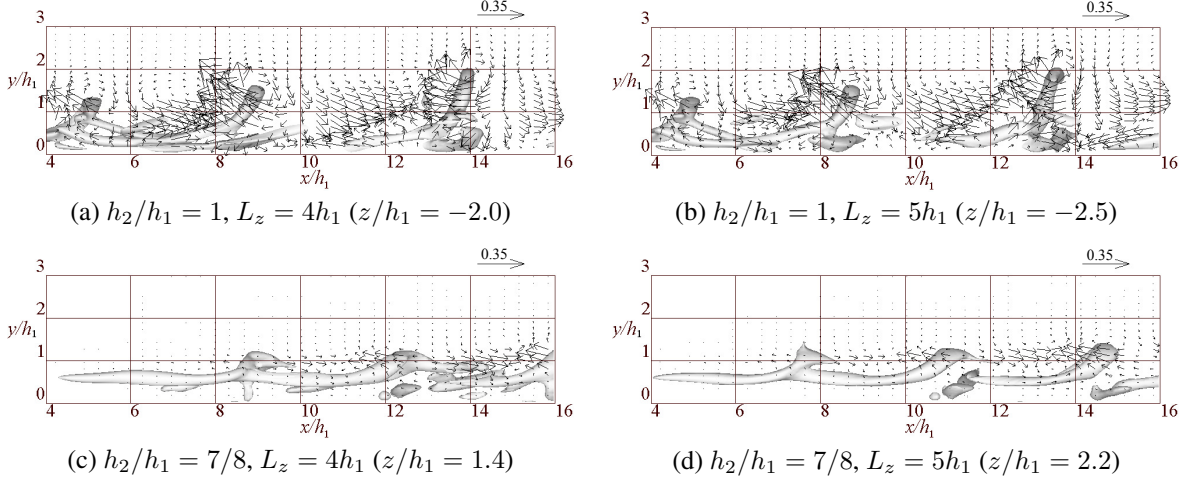


Figure 5: Isosurface of curvature of equipressure surface and velocity fluctuation vectors in x - y plane: Isosurface value is $-7/h_1$.

For $h_2/h_1 = 7/8$, the hairpin vortex shed from the hill at $z/h_1 \geq 0$ is smaller than the hairpin vortex at $z/h_1 < 0$. The small-scale hairpin vortex interferes with the large-scale hairpin vortex, so they have a stronger asymmetry than the hairpin vortex for $h_2/h_1 = 1$. Furthermore, when the hill spacing is narrowed, the leg on the spanwise center side of the small hairpin vortex does not extend. As shown in Fig. 3(d), behind the hill at $z/h_1 \geq 0$, the vorticity magnitude on the spanwise center side decreases due to the interference between the wakes, and the rollup of the vortex is weakened. Therefore, the leg on the spanwise center side in the small hairpin vortex does not develop downstream and decays immediately. As a result, that leg does not extend. For $h_2/h_1 = 7/8$ and $L_z = 5h_1$, unlike other conditions, the secondary vortex generated between both legs of the hairpin vortex at $z/h_1 < 0$ spreads above both legs in the spanwise direction when it moves downstream. For $h_2/h_1 = 7/8$ and $L_z = 4h_1$, a longitudinal vortex can be seen near the spanwise center. This longitudinal vortex is secondarily generated by large- and small-scale hairpin vortices and extends downstream toward the large-scale hairpin vortex. Therefore, it is considered that interference occurs downstream, even between this longitudinal vortex and the large-scale hairpin vortex.

The vortex shedding frequency of such a hairpin vortex was $f = 0.158U_\infty/h_1$ under all conditions. This value is close to the results, $f = 0.159U_\infty/h_1$ and $f = 0.163U_\infty/h_1$, at $Re = 500$ by the authors (Yanaoka et al., 2007a,b). In addition, this result exists in the range of the experimental results, $f = 0.13 - 0.25U_\infty/h_1$ and $f = 0.12 - 0.17U_\infty/h_1$, at $Re = 500$ by Acarlar and Smith (1987) and Sakamoto et al. (1987), respectively.

To observe the variations of the flow around the hairpin vortex with h_2/h_1 and L_z , Fig. 5 shows the isosurface of curvature of the equipressure surface and the velocity fluctuation vectors in the x - y plane. The results of $L_z = 4h_1$ and $5h_1$ for $h_2/h_1 = 1$ show the central cross-sections of the hills at $z/h_1 = -2.0$ and -2.5 , respectively. The results of $L_z = 4h_1$ and $5h_1$ for $h_2/h_1 = 7/8$ show the vicinity of the central cross-section of the hills at $z/h_1 = 1.4$ and 2.2 , respectively. As the tendency of the wake at $z/h_1 < 0$ of $L_z = 4h_1$ and $5h_1$ for $h_2/h_1 = 7/8$ is similar to the result of $L_z = 4h_1$ and $5h_1$ for $h_2/h_1 = 1$, the result is omitted here. In each case, a clockwise flow is induced around the head of the hairpin vortex. The phenomenon of flow from the lower side of the hairpin vortex head to the upstream mainstream side is called Q2 ejection, and the flow toward the downstream wall surface in front of the hairpin vortex head is called Q4 sweep (Yang et al., 2001).

For $h_2/h_1 = 1$, as shown around $y/h_1 = 1$ at $x/h_1 = 7 - 8$, an intensive shear layer occurs in the region where the flows generated by the Q2 ejection and Q4 sweep collide. This shear layer creates a secondary vortex between both legs. Around $x/h_1 = 14$ for $h_2/h_1 = 1$, a downward flow is generated by the horn-shaped secondary vortex. For $h_2/h_1 = 1$ and $L_z = 5h_1$, an ascending flow is locally generated near the wall surface at $x/h_1 = 12$. This is due to the rotation of the legs of the hairpin vortex. When the hill spacing is narrowed, the asymmetry of the hairpin vortices increases due to the strong interference between the hairpin vortices. As a result, because the leg of the hairpin vortex is closer to the central cross-section of the hill, the rotation of the leg affects the flow field over a wide range. Therefore, for $h_2/h_1 = 1$ and $L_z = 4h_1$, an ascending flow occurs over a wide area near the wall surface at $x/h_1 = 10 - 13$.

For $h_2/h_1 = 7/8$, as the velocity fluctuation around the head is smaller than the result for $h_2/h_1 = 1$, an intensive shear layer does not occur around the area where the flows generated by the Q2 ejection and Q4 sweep collide. Therefore,

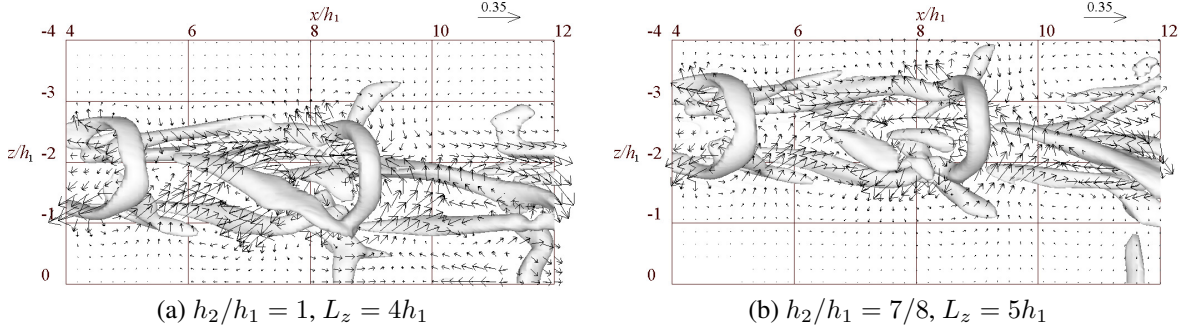


Figure 6: Isosurface of curvature of equipressure surface and velocity fluctuation vectors in x - z plane at $y/h_1 = 0.95$: Isosurface value is $-7/h_1$.

no secondary vortices are formed between both legs. Furthermore, the velocity fluctuation of the flow around the leg is smaller than that of the large-scale hairpin vortex generated under each condition.

To clarify the difference between the secondary vortices generated between both legs under each condition, Fig. 6 shows the isosurface of curvature of the equipressure surface and velocity fluctuation vectors in the x - z plane. Here, the results at $y/h_1 = 0.95$ for the cases of $h_2/h_1 = 1$, $L_z = 4h_1$, and $h_2/h_1 = 7/8$, $L_z = 5h_1$ in which a large difference appears in the secondary vortex are shown. For $h_2/h_1 = 1$ and $L_z = 4h_1$, as the hairpin vortices become asymmetric due to the interference between the hairpin vortices, the flow due to the Q2 ejection occurs toward the spanwise center side around $x/h_1 = 4 - 5$. At $x/h_1 = 5 - 7$, the asymmetry of the hairpin vortex structure increases due to the interference between the hairpin vortices, so the velocity fluctuation generated by the Q4 sweep on the spanwise center side increases. The collision of these flows generated by the upstream and downstream hairpin vortices causes the shear layer to become asymmetric to the center plane of the hill, and the secondary vortex seen at $x/h_1 = 6 - 8.5$ extends toward the spanwise center side. It can be seen that interference occurs between this secondary vortex and the leg on the spanwise center side and that the fluctuation of the flow to the upstream side is strong around $x/h_1 = 7$.

On the other hand, for $h_2/h_1 = 7/8$ and $L_z = 5h_1$, the interference between the hairpin vortices is weak, and the flow asymmetry becomes smaller than that for $h_2/h_1 = 1$ and $L_z = 4h_1$. A smaller secondary vortex than that for $h_2/h_1 = 1$ and $L_z = 4h_1$ is generated around $x/h_1 = 7$. Around $x/h_1 = 11$ downstream, two secondary vortices spread above the legs toward the spanwise direction. The behavior of this secondary vortex is similar to that of a secondary vortex generated around a single hairpin vortex (Yanaoka et al., 2007b).

4.3 Hairpin vortex and heat transport

To clarify heat transport around the hairpin vortex, Fig. 7 shows instantaneous vortex structures and turbulent heat flux vector $u_i'\theta'$ for $h_2/h_1 = 1$ and $L_z = 4h_1$. Figure 7(a) shows the heat flux around the head and leg of the hairpin vortex, and the arrows in this figure represent the heat flow around the hairpin vortex. Figure 7(b) shows the cross-section at $z/h_1 = 2.5$, where the heat flux outside the hairpin vortex and around the horn-shaped secondary vortex can be observed. From Fig. 7, we can see the magnitude and direction of heat transport due to the flow around the hairpin vortex. The tendency of heat transport was the same in all conditions, so the other results were omitted.

An upstream strong heat flux (H1) due to Q2 ejection around the hairpin vortex and heat flux (H2) to the mainstream side due to the legs and horn-shaped secondary vortices are generated, and active transport of hot fluid arises. Around the legs of the hairpin vortex, the high-temperature fluid transported by the ascending flow due to the rotation of the legs flows toward the wall surface outside of the legs. Around the legs on the spanwise center side in each hairpin vortex, because the turbulence increase due to interference between hairpin vortices and the flow toward the mainstream side due to secondary vortices occur, high-temperature fluid is transported more actively.

Figure 8 shows the distribution of temperature fluctuations in the x - y plane at the same z/h_1 as Fig. 5. Upstream of the head, positive fluctuations occur due to the transport of hot fluid by the Q2 ejection, and downstream of the head, negative fluctuations occur due to the inflow of cold fluid by the Q4 sweep. For $h_2/h_1 = 1$ and $L_z = 4h_1$, compared to the result of $L_z = 5h_1$, more intensive positive fluctuations are observed in a wide range of $x/h_1 = 5 - 7$, and $9 - 13$ near the wall surface, and heat transport becomes active. This is because the legs of the hairpin vortex remove the hot fluid near the wall surface upward. In the case of a single hairpin vortex (Yanaoka et al., 2007b), no such positive fluctuation was observed over a wide area near the wall surface.

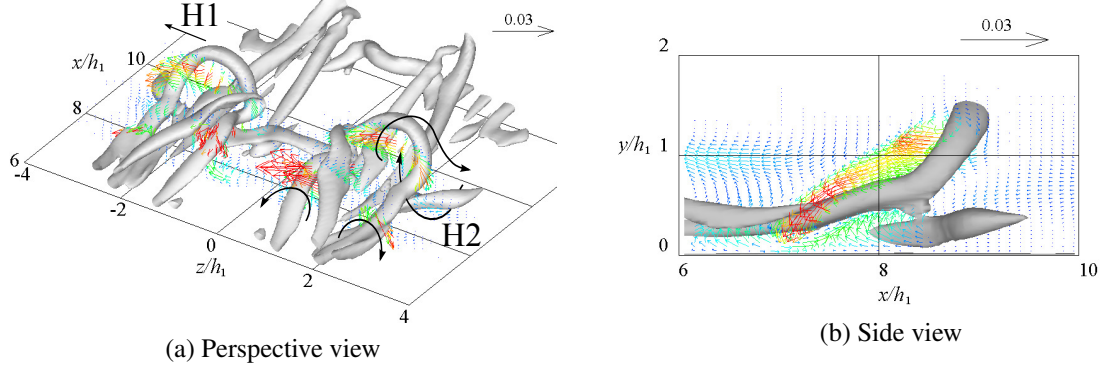


Figure 7: Isosurface of curvature of equipressure surface and turbulent heat flux vectors for $h_2/h_1 = 1$ and $L_z = 4h_1$: Isosurface value is $-7/h_1$.

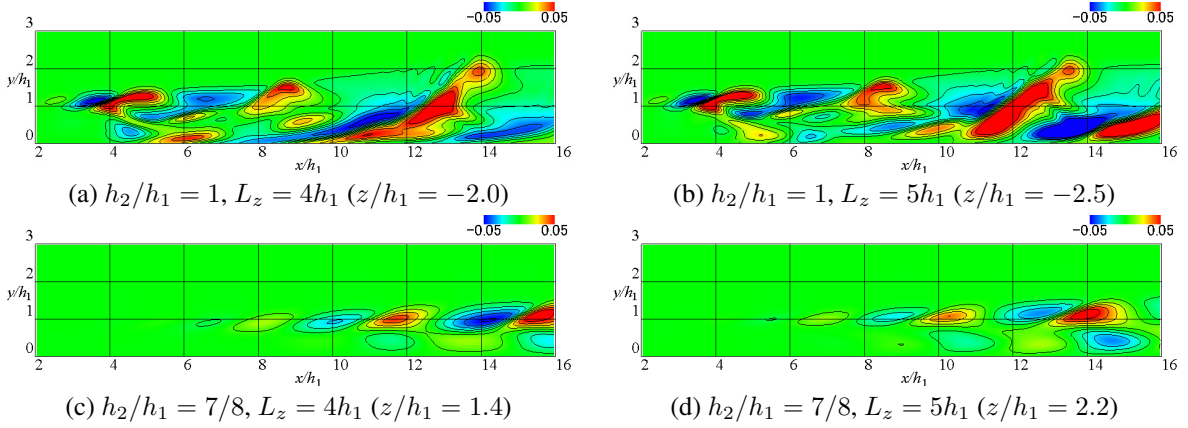


Figure 8: Contours of temperature fluctuation in x - y plane: Contour interval is 0.01 from -0.05 to 0.05 .

At $h_2/h_1 = 7/8$, as the rotation around the head is weaker than at $h_2/h_1 = 1$, the region of temperature fluctuation caused by the head becomes smaller. For $L_z = 5h_1$, the ascending flow by both legs is weak, and for $L_z = 4h_1$, the rotation of one leg of the hairpin vortex is weak, so no strong positive fluctuation occurs near the wall surface.

Next, Fig. 9 shows the fluctuation distribution of the Nusselt number in the x - z plane. In Fig. 5, the legs of the hairpin vortices existing at $x/h_1 = 6 - 8$ and $10 - 14$ form the ascending flow. Furthermore, as shown in Fig. 7, the legs and horn-shaped secondary vortices generate heat flux toward the mainstream side and transport the high-temperature fluid. Such a flow enhances heat transfer. Therefore, for all conditions, positive fluctuations occur around $x/h_1 = 8$ and 13 behind the hill at $z/h_1 < 0$. Negative fluctuations arise around $x/h_1 = 7, 10$, and 13 . This is because, as seen in Fig. 7, the high-temperature fluid transported by the legs flows toward the wall surface by the downward flow generated outside the legs. As a result, the heat transfer coefficient decreases. In the case of a single hairpin vortex (Yanaoka et al., 2008), the fluctuation distribution was symmetric to the central cross-section of the hill, but it is asymmetric in this study.

In the case of the same L_z , for $h_2/h_1 = 1$, as stronger interference between hairpin vortices occurs compared to $h_2/h_1 = 7/8$, high fluctuations appear on the spanwise center side. In each h_2/h_1 , when the hill spacing is narrowed, the interference between hairpin vortices becomes more intensive, so high fluctuations occur in the center of the spanwise direction, even downstream. In addition, the asymmetry of the hairpin vortex increases due to the intensive interference between hairpin vortices, and most of one leg at $z/h_1 < -2$ in the hairpin vortex approach the vicinity of the wall surface. As a result, the influence of the legs is widespread, and the positive fluctuation region around $z/h_1 = -2$ near $x/h_1 = 8$ and 13 increases. It will be described later that the turbulence near the wall surface increases due to the closeness of the legs.

For $h_2/h_1 = 7/8$, a weak fluctuation occurs behind the hill at $z/h_1 \geq 0$ due to a small-scale hairpin vortex. Around the small hairpin vortex, the ascending flow by the head and legs is weaker than that of the large-scale hairpin vortex. Therefore, heat transport decays and intensive fluctuations in heat transfer coefficient do not occur.

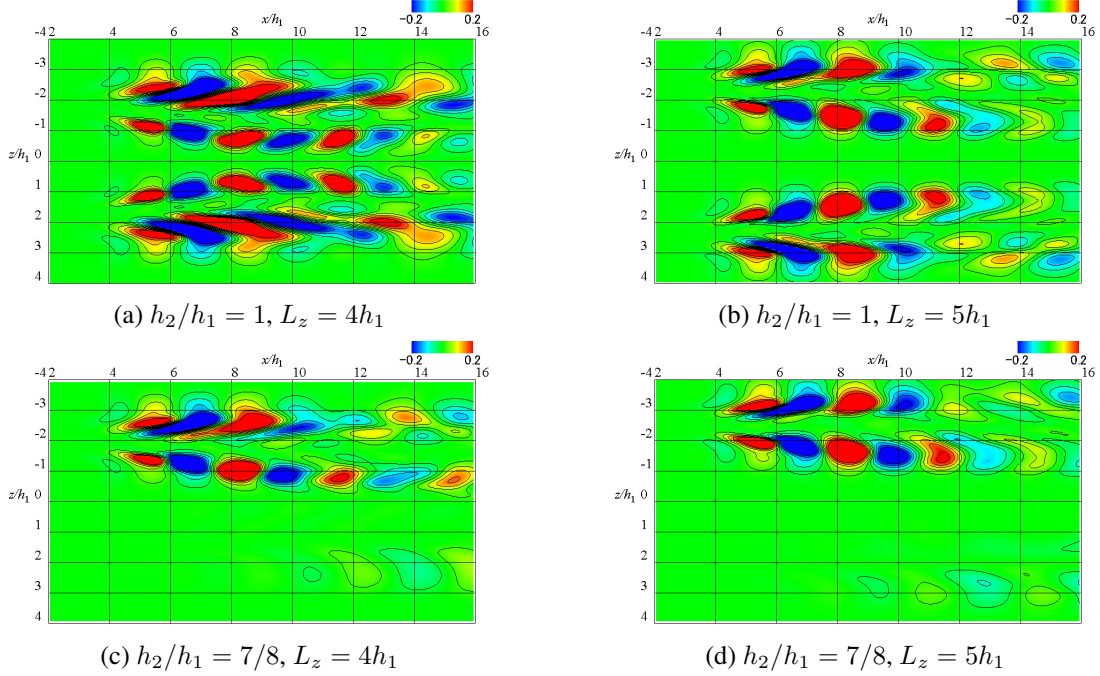


Figure 9: Contours of Nusselt number fluctuation in x - z plane: Contour interval is 0.04 from -0.2 to 0.2 .

4.4 Mean properties

Figure 10 shows the time-averaged streamwise velocity distribution \bar{u} for each condition. These distributions are the values in the central cross-section of the hill at $z/h_1 < 0$. All distributions are compared with the experimental values at $Re = 750$ by [Acarlar and Smith \(1987\)](#) and the calculations by the authors ([Yanaoka et al., 2007b](#)) for a single hairpin vortex. In the distribution of \bar{u} at $x/h_1 = 4$, the result of [Acarlar and Smith \(1987\)](#) shows no reverse flow. Conversely, the result of the authors ([Yanaoka et al., 2007b](#)) and this calculation show reverse flow in all distributions. At $x/h_1 = 10$, \bar{u} near the wall surface for $L_z = 4h_1$ is faster than the result for a single hairpin vortex ([Yanaoka et al., 2007b](#)) regardless of h_2/h_1 . In this study, the hairpin vortices become asymmetric due to the interference between the hairpin vortices. As a result, the leg of the hairpin vortex approaches the central cross-section of the hill, increasing \bar{u} near the wall surface. On the other hand, the result for $h_2/h_1 = 7/8$ and $L_z = 5h_1$ show almost the same velocity as that for a single hairpin vortex, indicating effects of interference between hairpin vortices are weak.

Figure 11 shows the distribution of \bar{u} obtained by the four grids for $h_2/h_1 = 1$ and $7/8$ at $L_z = 4h_1$. These distributions are the values in the central cross-section of the hill at $z/h_1 < 0$. We can confirm there is no intensive difference in the results depending on the number of grid points.

To investigate the effect of hairpin vortices on heat transfer, Fig. 12 shows the time-averaged Nusselt number \overline{Nu} in the central cross-section of the hill at $z/h_1 < 0$. All distributions are compared with the calculation result for a single hairpin vortex ([Yanaoka et al., 2007b](#)) and the value obtained from the similarity solution of the laminar boundary layer without flow separation ([Lighthill, 1950](#)). The similarity solution is given as $Nu = Nu_0/[1 - (s/x)]^{1/3}$ and $Nu_0 = 0.464Pr^{1/3}Re_x^{1/2}$, where s is the distance from the start point where the laminar boundary layer develops to the start point of heating, and in this study, $s = 10h_1$.

In all conditions, \overline{Nu} shows a lower value in the recirculation region than the similarity solution. Downstream from $x/h_1 = 5$, \overline{Nu} is higher than the similarity solution because the hairpin vortex increases heat transport. Downstream from $x/h_1 = 5$ at $h_2/h_1 = 1$ and $7/8$ for $L_z = 4h_1$, and downstream from $x/h_1 = 12$ and 14 at $h_2/h_1 = 1$ and $7/8$ for $L_z = 5h_1$, respectively, \overline{Nu} is higher than the result for a single hairpin vortex. In this study, the hairpin vortex becomes asymmetric due to the interference between hairpin vortices. As a result, \overline{Nu} increases because the leg and the horn-shaped secondary vortex pass near the central cross-section of the hill and remove the high-temperature fluid near the wall surface. This tendency is most prominent for $h_2/h_1 = 1$ and $L_z = 4h_1$, so \overline{Nu} at this condition is the highest among all results.

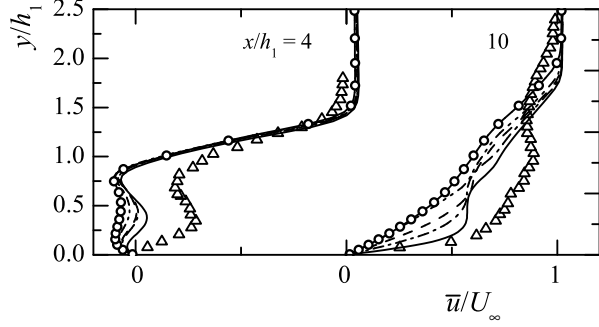
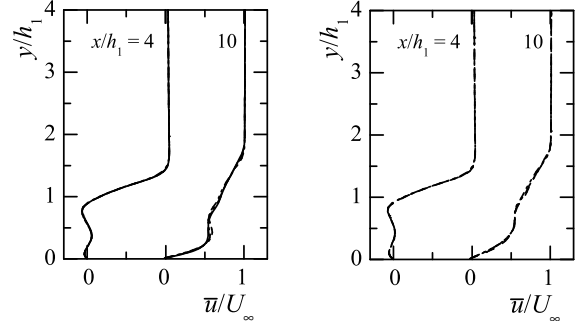


Figure 10: Time-averaged streamwise velocity distributions: —, $h_2/h_1 = 1$, $L_z = 4h_1$; ---, $h_2/h_1 = 1$, $L_z = 5h_1$; -·-, $h_2/h_1 = 7/8$, $L_z = 4h_1$; -··-, $h_2/h_1 = 7/8$, $L_z = 5h_1$; -○-, Yanaoka et al. ($Re = 500$); △, Acarlar-Smith ($Re = 750$).



(a) $h_2/h_1 = 1$, $L_z = 4h_1$ (b) $h_2/h_1 = 7/8$, $L_z = 4h_1$

Figure 11: Time-averaged streamwise velocity distributions: -··-, grid1; -·-, grid2; ---, grid3; —, grid4.

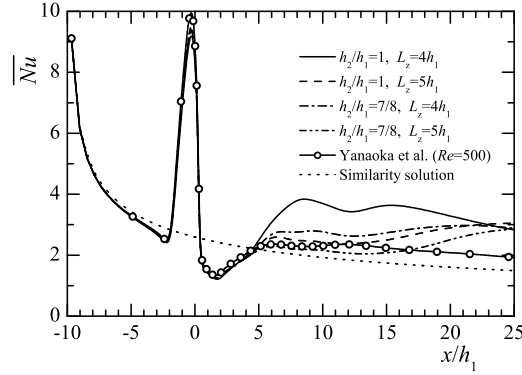


Figure 12: Time-averaged Nusselt number distributions.

4.5 Turbulence characteristics

The distributions of Reynolds stress $-\overline{u'v'}$ and turbulent heat flux $-\overline{u'\theta'}$ and $-\overline{v'\theta'}$ in the y - z plane at $x/h_1 = 8$ are shown in Fig. 13 to Fig. 15, respectively. Herein, for each region where a high turbulence region clearly appears, the turbulence region caused by the head of the hairpin vortex is labeled A. Other turbulence regions are labeled B for the leg and secondary vortex, C for the horn-shaped secondary vortex, and D for the horn-shaped secondary vortex and leg of the hairpin vortex. There are high turbulence regions due to the hairpin vortex behind the hill at $z/h_1 < 0$ for all distributions. The turbulence distribution is asymmetric to the center cross-section of the hill, unlike the distribution for a single hairpin vortex (Yanaoka et al., 2007b). This is because vortex structures become asymmetric to the center cross-section of the hill due to the interference between hairpin vortices. In turbulence region A caused by the head of the hairpin vortex, there is no significant increase in turbulence due to changes in the scale ratio of the hills or the hill spacing.

In all distributions, as interference between hairpin vortices occurs, the turbulence (region B) due to the leg and secondary vortex and turbulence (region C) due to the horn-shaped secondary vortex are high, and heat transport is active in regions B and C. This tendency appears strongly when the hill spacing is narrowed, regardless of h_2/h_1 , and is most remarkable at $h_2/h_1 = 1$ and $L_z = 4h_1$. Furthermore, for $h_2/h_1 = 1$ and $L_z = 4h_1$, a high turbulence region extends to the spanwise center because the horn-shaped secondary vortices are connected. For $h_2/h_1 = 1$ and $L_z = 5h_1$, the horn-shaped secondary vortices are not coupled at $x/h_1 = 8$, so the high turbulence region does not extend to the spanwise center. At $h_2/h_1 = 7/8$, it can be seen that the turbulence due to the small-scale hairpin vortex is low, and the heat transport decays behind the hill at $z/h_1 \geq 0$.

When the hill spacing is narrowed, the turbulence region C due to the horn-shaped secondary vortex in $-\overline{u'\theta'}$ and the turbulence region D due to the horn-shaped secondary vortex and legs in $-\overline{v'\theta'}$ approach the central cross-section of

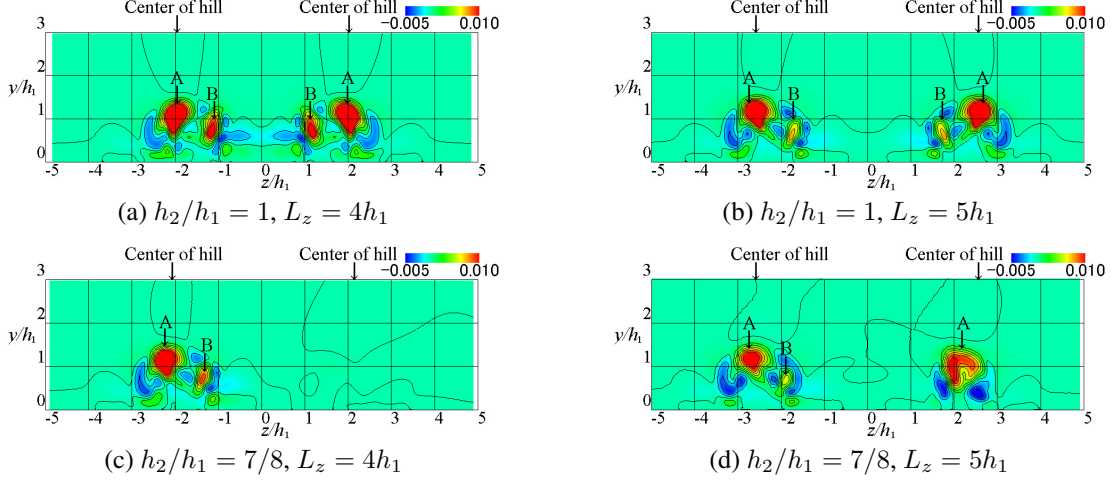


Figure 13: Contours of Reynolds shear stress $-\overline{u'v'}$ in y - z plane at $x/h_1 = 8.0$: Contour interval is 0.0015 from -0.005 to 0.010 .

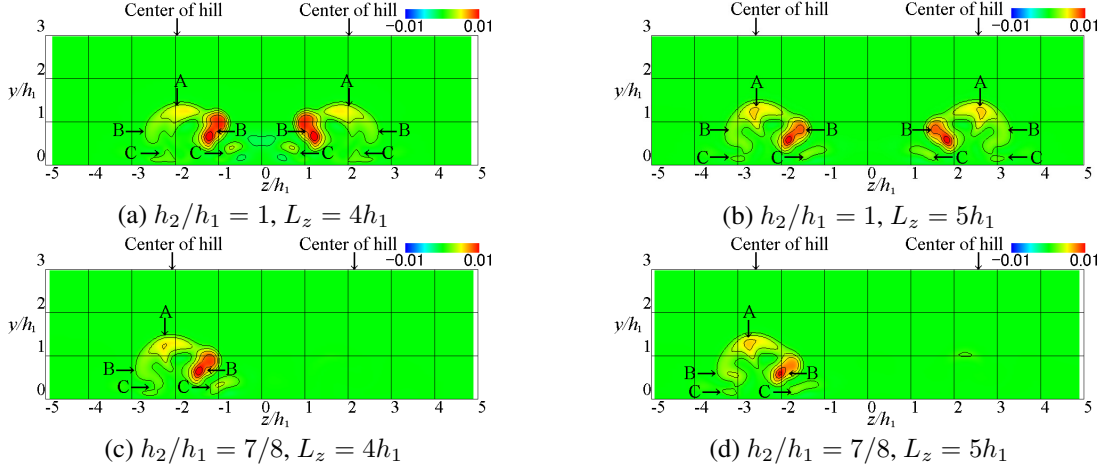


Figure 14: Contours of turbulent heat flux $-\overline{u'\theta'}$ in y - z plane at $x/h_1 = 8.0$: Contour interval is 0.002 from -0.01 to 0.01 .

the hill because the asymmetry of vortex structures increases. Therefore, around the central cross-section of the hill, heat transport becomes active due to the horn-shaped secondary vortex and leg of the hairpin vortex.

Figure 16 shows the distributions in the z -direction for the rms value u_{rms} of the streamwise velocity fluctuation and the turbulent heat flux $-\overline{u'\theta'}$. The positions in the y -direction are $y/h_1 = 0.65$ and 0.6 for $L_z = 4h_1$ and $5h_1$ at $h_2/h_1 = 1$, respectively, and $y/h_1 = 0.65$ and 0.6 for $L_z = 4h_1$ and $5h_1$ at $h_2/h_1 = 7/8$, respectively. These positions are the cross-sections where u_{rms} shows the highest turbulence value at the leg of the hairpin vortex for each h_2/h_1 and L_z . The central cross-section of the hill at $z/h_1 < 0$ is $z_c/h_1 = 0$. For all distributions, the distribution obtained from the data for a single hairpin vortex (Yanaoka et al., 2007b) is symmetric to the central cross-section of the hill. At $x/h_1 = 4$, u_{rms} for each condition is at the same level as that for a single hairpin vortex. At $x/h_1 = 8$, u_{rms} on the spanwise center side at $z_c/h_1 > 0$ increases, and the distribution becomes asymmetric, indicating that interference between hairpin vortices occurs. On the spanwise center side, $-\overline{u'\theta'}$ is also high, indicating active heat transport. At that time, the values of all turbulences are higher than that for a single hairpin vortex.

Compared with the result of $h_2/h_1 = 7/8$, u_{rms} on the spanwise center side at $h_2/h_1 = 1$ is higher, and the distribution asymmetry is also larger. It can be seen from this that the interference between hairpin vortices with the same scale strongly appears. In the distribution of $-\overline{u'\theta'}$, the same tendency as u_{rms} can be observed, and heat transport on the spanwise center side at $h_2/h_1 = 1$ is active.

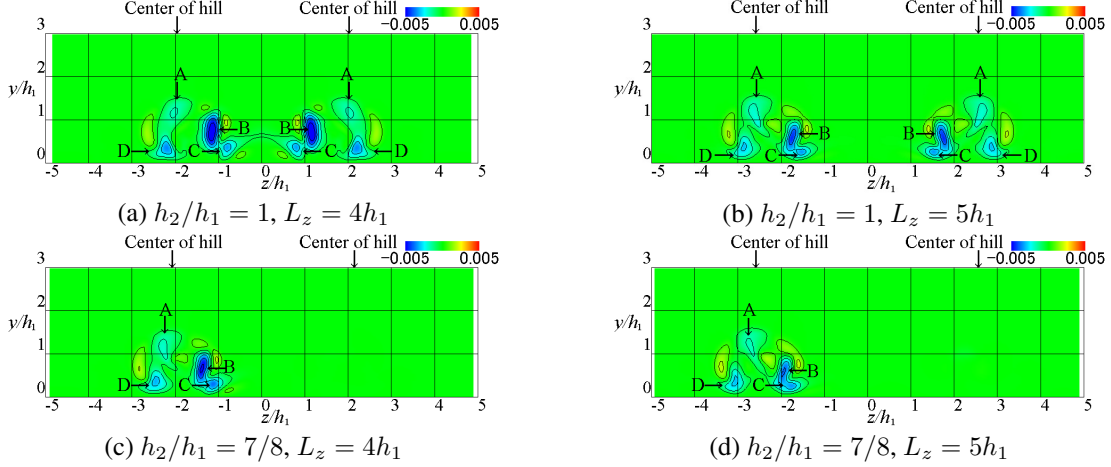


Figure 15: Contours of turbulent heat flux $-\overline{v'\theta'}$ in y - z plane at $x/h_1 = 8.0$: Contour interval is 0.001 from -0.005 to 0.005.

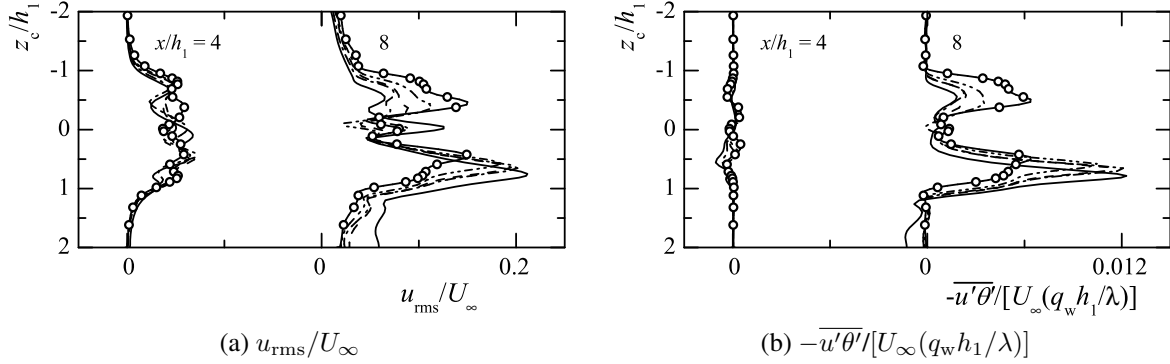


Figure 16: Turbulence intensity distributions of streamwise velocity fluctuation and distribution of turbulent heat flux: —, $h_2/h_1 = 1, L_z = 4h_1$; ---, $h_2/h_1 = 1, L_z = 5h_1$; -·-, $h_2/h_1 = 7/8, L_z = 4h_1$; -··-, $h_2/h_1 = 7/8, L_z = 5h_1$; -○-, Yanaoka et al. ($Re = 500$).

When the hill spacing is narrowed, the interference between hairpin vortices is more intensive, and u_{rms} on the spanwise center side increases. For $h_2/h_1 = 7/8$ and $L_z = 4h_1$, as a longitudinal vortex is generated on the spanwise center side, the interference between the hairpin vortex and longitudinal vortex also increases u_{rms} . As the value on the spanwise center side of $-\overline{u'\theta'}$ also increases, it can be seen that the heat transport improves when the interference between hairpin vortices becomes stronger.

Figure 17(a) shows the turbulence distribution in the central cross-section of the hill at $z/h_1 < 0$. Figure 17(b) shows the enlarged distribution near the wall surface at $x/h_1 = 10$ in Fig. 17(a). The results of this calculation are compared with the experimental values of Acarlar and Smith (1987) and the calculation results for a single hairpin vortex by the authors (Yanaoka et al., 2007b). At $x/h_1 = 4$, two maxima are observed in this calculation for all conditions and in the previous results (Acarlar and Smith, 1987; Yanaoka et al., 2007b). The maximum value on the mainstream side is due to the head of the hairpin vortex. The maximum value near the wall surface seen in the previous result (Acarlar and Smith, 1987) is due to the leg of the hairpin vortex. On the other hand, as the maximum value in this calculation occurs near $y/h_1 = 0.75$ below the head of the hairpin vortex, this turbulence at the wall side is due to the Q2 ejection of the hairpin vortex.

At $x/h_1 = 10$ for $h_2/h_1 = 1$, the turbulence caused by the head of the hairpin vortex decays faster than the result for a single hairpin vortex, and a high maximum value of turbulence occurs near the wall surface. Then, u_{rms} for $L_z = 4h_1$ has a higher value than for $L_z = 5h_1$. When the hill spacing is narrowed, the asymmetry of the vortex structure increases as the interference between hairpin vortices increases. As a result, u_{rms} increases because the horn-shaped secondary vortex and the leg of the hairpin vortex are closer to the central cross-section of the hill.

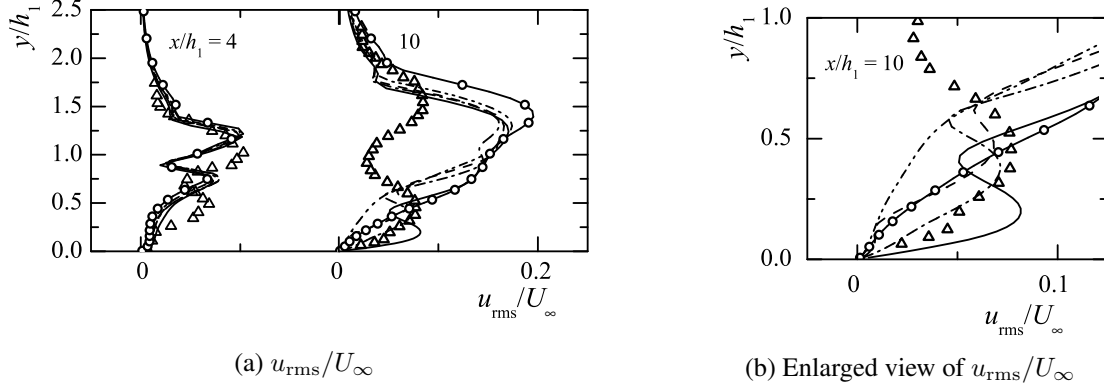


Figure 17: Turbulence intensity distributions of streamwise velocity fluctuation: —, $h_2/h_1 = 1, L_z = 4h_1$; ---, $h_2/h_1 = 1, L_z = 5h_1$; - · -, $h_2/h_1 = 7/8, L_z = 4h_1$; - · · -, $h_2/h_1 = 7/8, L_z = 5h_1$; -○-, Yanaoka et al. ($Re = 500$); △, Acarlar-Smith ($Re = 750$).

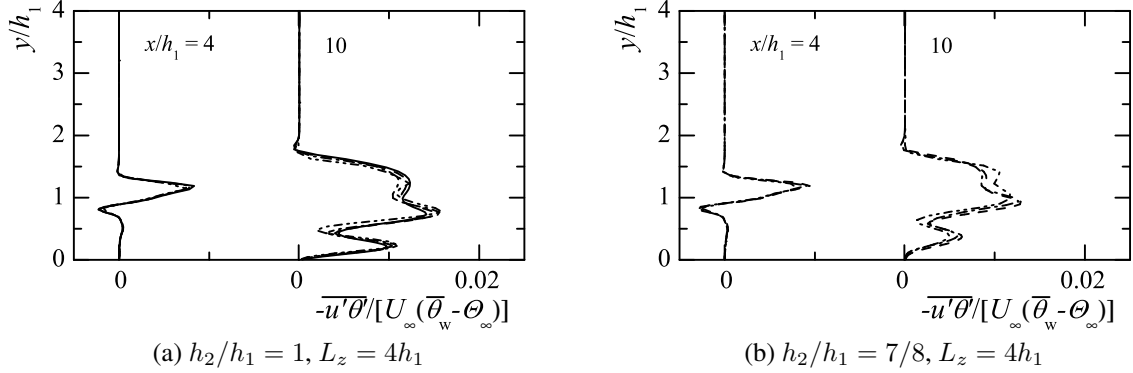


Figure 18: Distributions of turbulent heat flux: - · · · -, grid1; - · · -, grid2; ---, grid3; —, grid4.

For $h_2/h_1 = 7/8$ and $L_z = 4h_1$, high turbulence appears near the wall surface at $x/h_1 = 10$, similar to $h_2/h_1 = 1$. This is because the horn-shaped secondary vortex and the leg of the hairpin vortex approach the central cross-section of the hill as the hairpin vortex structure becomes asymmetric due to the interference between hairpin vortices and interference between the hairpin vortex and longitudinal vortex. For $h_2/h_1 = 7/8$ and $L_z = 5h_1$, as the influence of interference between hairpin vortices is weak, the asymmetry of the hairpin vortex structure is small. Therefore, the result of this calculation is qualitatively similar to that for a single hairpin vortex.

Focusing on Fig. 17(b), the maximum value for $h_2/h_1 = 1$ and $L_z = 4h_1$ occurs closer to the wall surface than other results. It can be seen from this that the leg of the hairpin vortex approaches the wall surface as a result of the increase in the asymmetry of the hairpin vortex due to the interference between hairpin vortices.

Figure 18 shows the distribution of the turbulent heat flux $-u'\theta'$ obtained by the four grids for $h_2/h_1 = 1$ and $7/8$ at $L_z = 4h_1$. These distributions are the values in the central cross-section of the hill at $z/h_1 < 0$. For $h_2/h_1 = 1$ and $L_z = 4h_1$, there is a difference between the result of grid4 and the results of grid1 and grid2, but the results of grid4 and grid3 agree well. For $h_2/h_1 = 7/8$ and $L_z = 4h_1$, there is a difference between the results of grid3 and grid1, but the results of grid3 and grid2 agree well. From the above results, it is considered that grid4 and grid3 used in the calculations of $h_2/h_1 = 1$ and $7/8$ for $L_z = 4h_1$ have sufficient grid resolution, respectively.

5 Conclusions

We performed a numerical analysis of the hairpin vortex and heat transport generated by the interference of the wakes behind two hills in a laminar boundary layer. As a result, the following results were obtained.

When hills with the same scale are installed, hairpin vortices with the same scale are periodically shed behind the hills symmetrically with respect to the spanwise center. The hairpin vortex becomes asymmetric downstream. Hairpin

vortices with different scales periodically occur behind the different-scale hills. In the case of hills with the same scale, the interference between hairpin vortices in the wake is stronger than in the different-scale hills. When the hill spacing in the spanwise direction is narrowed, the asymmetry of the hairpin vortex in the wake increases due to the interference between the wakes.

High turbulence areas occur around the head and both legs of the hairpin vortex, and the turbulence due to the horn-shaped secondary vortex occurs near the wall surface. Regardless of the scale ratio of the hills, when the hill spacing is narrowed, the significant interference between hairpin vortices increases the turbulence due to the leg and horn-shaped secondary vortex on the spanwise center side in the hairpin vortex, resulting in active heat transport around the hairpin vortex. In addition, the strong interference between hairpin vortices increases the asymmetry of the hairpin vortex, and the leg of the hairpin vortex approaches the wall surface. As a result, the leg removes high-temperature fluid near the wall surface over a wide area, improving heat transfer. These tendencies are most remarkable in the same-scale hills.

Around the hills with different scales, if the hill spacing is narrowed, the vortex size on the spanwise center side in the vortex pair generated behind the small hill becomes smaller due to the interference between the wakes. As a result, as the rollup of the vortex on the spanwise center side is weakened, the leg on the spanwise center side in a small hairpin vortex does not develop downstream and decays quickly. Due to the attenuation of the leg, heat transport around the hairpin vortex decays, and the heat transfer coefficient significantly decreases.

Acknowledgements. The numerical results in this research were obtained using supercomputing resources at the Cyberscience Center, Tohoku University. This research did not receive any specific grant from funding agencies in the public, commercial, or not-for-profit sectors. We would like to express our gratitude to Associate Professor Yosuke Suenaga of Iwate University for his support of our laboratory. The authors wish to acknowledge the time and effort of everyone involved in this study.

Declaration of interests. The authors report no conflicts of interest.

Author ORCID.

H. Yanaoka <https://orcid.org/0000-0002-4875-8174>.

Author contributions. H. Yanaoka conceived and planned the research and developed the computational method and numerical codes. T. Hamada performed the simulations. All authors contributed equally to analyzing data, reaching conclusions, and writing the paper.

References

- Acarlar, M.S., Smith, C.R., 1987. A study of hairpin vortices in a laminar boundary layer. Part 1. Hairpin vortices generated by a hemisphere protuberance. *J. Fluid Mech.* 175, 1–41. doi:doi:<https://doi.org/10.1017/S0022112087000272>.
- Amsden, A.A., Harlow, F.H., 1970. A simplified MAC technique for incompressible fluid flow calculations. *J. Comput. Phys.* 6, 322–325. doi:doi:[https://doi.org/10.1016/0021-9991\(70\)90029-X](https://doi.org/10.1016/0021-9991(70)90029-X).
- Dong, S., Meng, H., 2004. Flow past a trapezoidal tab. *J. Fluid Mech.* 510, 219–242. doi:doi:<https://doi.org/10.1017/S0022112004009486>.
- Elavarasan, R., Meng, H., 2000. Flow visualization study of role of coherent structures in a tab wake. *Fluid Dyn. Res.* 27, 183–197. doi:doi:[https://doi.org/10.1016/s0169-5983\(00\)00003-4](https://doi.org/10.1016/s0169-5983(00)00003-4).
- Ko, N.W.M., Wong, P.T.Y., Leung, R.C.K., 1996. Interaction of flow structures within bistable flow behind two circular cylinders of different diameters. *Exp. Therm. Fluid Sci.* 12, 33–44. doi:doi:[https://doi.org/10.1016/0894-1777\(95\)00065-8](https://doi.org/10.1016/0894-1777(95)00065-8).
- Kurita, E., Yahagi, Y., 2008. Vortex structure behind highly heated two cylinders in parallel arrangements. *JSME, Ser. B* 74, 1600–1608. doi:doi:<https://doi.org/10.1002/htj.20244>. (in Japanese).
- Li, H., Yu, T., Wang, D., Xu, H., 2019. Heat-transfer enhancing mechanisms induced by the coherent structures of wall-bounded turbulence in channel with rib. *Int. J. Heat Mass Transf.* 137, 446–460. doi:doi:<https://doi.org/10.1016/j.ijheatmasstransfer.2019.03.122>.
- Lighthill, M.J., 1950. Contributions to the theory of heat transfer through a laminar boundary layer. *Proc. R. Soc. Lond. A* 202, 359–377. doi:doi:<https://doi.org/10.1098/rspa.1950.0106>.

- Meinders, E.R., Hanjalić, K., 2002. Experimental study of the convective heat transfer from in-line and staggered configurations of two wall-mounted cubes. *Int. J. Heat Mass Transf.* 45, 465–482. doi:doi:[https://doi.org/10.1016/S0017-9310\(01\)00180-6](https://doi.org/10.1016/S0017-9310(01)00180-6).
- Rhie, C.M., Chow, W.L., 1983. Numerical study of the turbulent flow past an airfoil with trailing edge separation. *AIAA J.* 21, 1525–1532. doi:doi:<https://doi.org/10.2514/3.8284>.
- Sakamoto, H., Haniu, H., Obata, Y., 1987. Vortex shedding from a circular cylinder placed vertically in a laminar boundary layer. *JSME, Ser. B* 53, 714–721. doi:doi:<https://doi.org/10.1299/KIKAIB.53.714>. (in Japanese).
- Simpson, R.L., Long, C.H., Byun, G., 2002. Study of vortical separation from an axisymmetric hill. *Int. J. Heat Fluid Flow* 23, 582–591. doi:doi:[https://doi.org/10.1016/S0142-727X\(02\)00154-6](https://doi.org/10.1016/S0142-727X(02)00154-6).
- Sumner, D., Wong, S.S.T., Price, S.J., Paidoussis, M.P., 1999. Fluids behavior of side-by-side circular cylinders in steady cross-flow. *J. Fluids Struct.* 13, 309–338. doi:doi:<https://doi.org/10.1006/jfls.1999.0205>.
- Yanaoka, H., Inamura, T., Kawabe, S., 2007a. Numerical simulation of behavior and heat transfer of hairpin vortices generated around a cube in a laminar boundary layer. *JSME, Ser. B* 73, 268–275. doi:doi:<http://dx.doi.org/10.1299/kikaib.73.268>. (in Japanese).
- Yanaoka, H., Inamura, T., Suenaga, Y., Abe, K., 2008. Numerical analysis of the effect of boundary layer thickness on vortex structures and heat transfer in the wake behind a hill. *Heat Trans. Asian Res.* 38, 435–449. doi:doi:<https://doi.org/10.1002/htj.20261>.
- Yanaoka, H., Inamura, T., Suenaga, Y., Kobayashi, Y., 2007b. Numerical simulation of vortex structures and heat transfer behind a hill in a laminar boundary layer. *JSME, Ser. B* 73, 2357–2544. doi:doi:<https://doi.org/10.1299/kikaib.73.2537>. (in Japanese).
- Yang, W., Meng, H., Sheng, J., 2001. Dynamics of hairpin vortices generated by a mixing tab in a channel flow. *Exp. Fluids* 30, 705–722. doi:doi:<https://doi.org/10.1007/s003480000252>.